Bibliographical reference

Equivalent Source Method and Boundary Element Method for Calculating Combustion Noise, Rafael Piscoya, Haike Brick, Martin Ochmann and Peter Költzsch, Acta Acustica **vol. 94** (Number 4), 2008, pp. 514-527

DOI

https://doi.org/10.3813/AAA.918060

Acta Acustica united with Acustica
Vol. 94 (2008) 514 – 527

DOI 10.3813/AAA.918060

Equivalent Source Method and Boundary Element Method for Calculating Combustion Noise

Rafael Piscoya, Haike Brick, Martin Ochmann
University of Applied Sciences Berlin, 13353 Berlin, Germany

Peter Költzsch
Technical University Dresden, 01062 Dresden, Germany

Summary
In this paper, the application of the Equivalent Source Method (ESM) and the acoustical Boundary Element Method (BEM) for the prediction of the noise generated by an open diffusion flame is investigated. These acoustical methods have been coupled with a Large Eddy Simulation (LES) of the turbulent flow, which simulates the flow and combustion processes in a source region in the vicinity of the flame. Among the hybrid methods which are being used to predict the sound produced by turbulent flow, the ESM and BEM have the advantage that only one acoustic variable must be known at a surface surrounding the source zone (fewer data has to be processed) and that the far field can be directly computed. The sound power generated from two open diffusion flames have been calculated with both the ESM and the BEM, using the velocity distribution over cylindrical control surfaces, which enclose the source region. The results of the calculations are presented and compared with the measured sound power of the same flames. For one configuration good agreement between measurement and simulation at low and middle frequencies is obtained. Possible reasons for the differences for the other configuration will be discussed.

PACS no. 43.20.Rz, 43.28.Kt, 43.28.Ra

1. Introduction

Hybrid methods, coupling CFD (Computational Fluid Dynamics) codes with acoustic methods like Lighthill's acoustic analogy, the linearized Euler equations or the Kirchhoff method are used to predict the sound produced by a turbulent flow, since the present computational power only allows an accurate estimation of the physical quantities in reasonable computational time in a domain near the source. This means that the acoustic far field cannot be determined by a CFD simulation. Hybrid methods, in which the turbulent flow in the source region and the acoustic far field are computed separately, are able to solve such complex problems. Lighthill's acoustic analogy provides a procedure to compute the far field but requires the evaluation of a volume integral. This task often consumes a lot of time and storage capacity. The linearized Euler equations need to discretize the time and the three-dimensional space, which prevents extending the computational domain to the far field. The Kirchhoff method involves, in contrast, less computational costs since a surface integral has to be solved and allows also the determination of the far field. Due to this reason, the method has become very popular recently. A substantial review of hybrid methods for aero acoustic computations with a focus on surface integral methods is given by Lyrintzis [1]. More recent studies confirm the effectiveness of surface integral methods. For example, Uzun *et al.* [2] show that surface integral methods give similar results to the volume integral method at a much lower cost, Rahier *et al.* [3] develop a Kirchhoff method using two types of input data, density and pressure, and found that the pressure was more suitable for jet noise prediction. Andersson *et al.* [4] obtain very accurate sound pressure level for an isothermal and a hot jet up to a Strouhal number of 1.2 utilizing the Kirchhoff surface integration.

In the present work, we study the application of a hybrid technique to reactive turbulent flows, particularly to open turbulent flames. The strategy remains the same, the non- linear region including the combustion zone is treated with the CFD code whereas the sound radiation is computed with a pure acoustical method. The novelty of our technique is the use of two well known methods of technical acoustics, the ESM and the BEM, as acoustic coupling methods. Both methods have the homogeneous Helmholtz equation as starting point and only require one acoustic variable on a control surface, which is directly taken from the CFD calculation. This control surface (Kirchhoff sur-

Received 23 November 2006,
accepted 13 April 2008.

face) must enclose all sound sources and lie in a homogeneous medium.

The BEM has been used in aeroacoustics, for example to describe the aero acoustics of wings and rotors [5, 6, 7] and for computing scattered sound [8] and noise from engine inlets [9]. When in-duct acoustic propagation has been simulated, CFD solutions were expanded into spinning and radial modes and converted into equivalent monopoles. These adapted monopoles were used as input sources into the BEM code to compute the radiated field. For exterior problems like diffraction by solid boundaries or trailing edge noise, the acoustic analogy has been used to determine the strength of equivalent surface distributed dipoles and volume distributed quadrupoles and the sound field was then obtained using a direct BEM. In our study of the open flames, the velocity distribution at the Kirchhoff surface serves as input data for the BEM code.

The ESM is a technique that have been successfully used to describe the sound radiation of vibrating bodies and the sound scattered from solid structures in a homogeneous and quiescent medium. It consists in replacing the original sound source with a collection of simple sources that reproduce a given boundary condition. Different types of problems have been treated with this method, from relatively simple geometries up to bodies with complex shapes, from radiation into free space to radiation in enclosures. Most developed algorithms work in the frequency domain but there are also procedures working in the time domain. Efforts have been made to develop methods to optimize the position of the equivalent sources, since the ESM does not specify these positions, which can have an important influence on the accuracy of the results, see references [10]–[22].

An extension of the application of equivalent sources to aeroacoustic problems was made by Holste [23] who used the method to predict the radiated sound field of a prop fan model. He used ring sources for his calculations, due to the circular geometry of the prop fan, and values of pressure measured behind the exit plane to determine the amplitude of the ring sources. The presence of the flow was directly taken into account, since the radiated sound field of the ring sources was derived using a convective flow equation. We intend to extend the application of the ESM to aero-thermo acoustic problems, using equivalent sources that are solutions of the homogeneous Helmholtz equation without flow. These solutions are considered to be appropriate if the Mach number of the fluid motion is small and the surface, where the boundary condition is given, is far away enough from the combustion zone, so that the non-linearities can be neglected.

We begin with a short description of each of the methods, referring to the literature for further details. In section 3, a brief description of the studied flame is given. The preparation of the input data and the generation of the acoustic model are detailed in section 4. The validation of the hybrid method is made by comparing the simulated results with measurements of the flames in sections 5 and 6.

2. Theory

2.1. ESM

The principle of the ESM is to replace the original sound source with a system of equivalent multipoles whose amplitudes are determined in such a way that a boundary condition is satisfied [15]. When the boundary condition is exactly reproduced by the equivalent sources, their radiated sound is identical to the sound radiated by the original source. Normally the boundary condition is not completely fulfilled and an error arises. The strengths of the multipoles are determined in such a way, that this error is minimized.

The simplest equivalent sources are described by spherical wave functions, which are solutions of the Helmholtz equation and satisfy the Sommerfeld radiation condition at infinity. The most general expression for the sound pressure generated by Q multipole sources with order up to N, which are located in the positions given by the vectors $\vec{r}_q$, is

$$p(\vec{r}) = \sum_{q=1}^{Q}\sum_{n=0}^{N}\sum_{m=0}^{n} \frac{h_n^{(2)}\left(k|\vec{r}-\vec{r}_q|\right)}{h_n^{(2)}\left(kR\right)} P_n^m(\cos\gamma_q) \cdot \left(A_{nm}^{(q)}\cos(m\delta_q) + B_{nm}^{(q)}\sin(m\delta_q)\right), \quad (1)$$

where P_n^m are the Legendre functions, $h_n^{(2)}$ are spherical Hankel functions of the second kind and γ_q and δ_q are the angles between the vector $(\vec{r}-\vec{r}_q)$ and the z- and x-axis respectively. The spherical wave functions in equation (1) have been normalized using $h_n^{(2)}(kR)$, R being a typical dimension of the source. This normalization brings a favorable effect in the numerical operations involving the system matrix. The total number of spherical functions and thus the number of equivalent sources in expression (1) is $N_{\text{tot}} = Q(N+1)^2$. For simplicity, equation (1) is written as

$$p(\vec{r}) = \sum_{i=1}^{N_{\text{tot}}} c_i \psi_i(\vec{r}), \quad (2)$$

where the subindex i represents a combination of q, n and m, and c_i and ψ_i are the amplitude and wave function for that q, n, m combination.

The amplitudes c_i are determined by minimizing the velocity error at the control surface (ε) using the method of weighted residuals [20]. The velocity error is defined as

$$\varepsilon = \frac{\mathrm{j}}{\omega\rho}\sum_{i=1}^{N_{\text{tot}}} c_i \frac{\partial\psi_i}{\partial n} - v_{nS}, \quad (3)$$

where v_{nS} is the known velocity distribution. The boundary error ε is multiplied by weighting functions w_l and the integral of the product over the surface S is set to zero. This yields the following equations

$$\frac{\mathrm{j}}{\omega\rho}\sum_{i=1}^{N_{\text{tot}}} c_i \int_S \frac{\partial\psi_i}{\partial n} w_l \,\mathrm{d}S = \int_S v_{nS} w_l \,\mathrm{d}S, \quad (4)$$

$l = 1, 2, \ldots, N_{\text{tot}}$. The weighting functions used for the calculations are the complex conjugate normal derivatives of the wave functions $w_l = \partial\psi_l^*/\partial n$. The selection of these functions implies a minimization of the velocity error in the least square sense. With the discretization of the surface and assuming constant values over each element, equation (4) is transformed into a system of linear equations $\boldsymbol{Ax} = \boldsymbol{b}$ that has to be solved. $\boldsymbol{A}$ is a $N_{\text{tot}} \times N_{\text{tot}}$ matrix and $\boldsymbol{x}$ is the vector of amplitudes c_i.

Once the strengths c_i are known, the sound field can be computed at any point outside S using (2). All other related acoustic quantities like particle velocity, intensity and power are directly derived from (2).

2.2. BEM

The fundamental derivations of the boundary element method in acoustics can be found for example in [24, 25, 26]. Here merely a brief outline of the used BE technique is given.

In our paper, the direct BEM approach is applied. Starting point of the direct BEM is the Helmholtz integral equation (HIE) for exterior field problems,

$$\iint_S \left[p(y)\frac{\partial g(x,y)}{\partial n(y)} - \frac{\partial p(y)}{\partial n(y)}g(x,y)\right] \mathrm{d}s = C(x)p(x), \quad (5)$$

where

$$g(x,y) = \frac{\mathrm{e}^{-\mathrm{j}kr}}{4\pi r} \quad \text{and} \quad r = r(x,y) = ||y - x|| \quad (6)$$

is the Greens function in the three dimensional free space. $C(x)$ equals 1 for x in the acoustic domain, i.e. in the exterior domain, 1/2 on the surface of the radiating structure and 0 for x in the interior domain. Since a Neumann boundary condition is considered (the normal velocity v_n is prescribed on the surface) equation (5) becomes

$$\iint_S \left[p(y)\frac{\partial g(x,y)}{\partial n(y)} + \mathrm{j}\omega v_n g(x,y)\right] \mathrm{d}s = C(x)p(x). \quad (7)$$

The surface is discretized by a set of constant elements, i.e. the conversion of the Helmholtz integral equation into a corresponding system of equations is derived by approximating the boundary function on each surface element by a constant value. The accuracy of the approximation is assured by the six-element-per-wavelength rule [27]. The system of equations is set up by the collocation method. The diagonal elements of the resulting matrices, which become singular, are treated as it is described in [25].

The Helmholtz integral equation (5) for an exterior Neumann problem, where $\partial p(y)/\partial n(y)$ is prescribed on the surface of the radiating structure, does not have a unique solution at the characteristic eigenfrequencies of the associated interior Dirichlet problem. To avoid the non-uniqueness of the system of equations at these eigenfrequencies the CHIEF-method (Combined Helmholtz Integral Equation Formulation) was applied, which was suggested by Schenck [28]. Here additional collocation points (the CHIEF-points) are located in the interior domain of the object, where the interior Helmholtz integral formulation must be satisfied. With this overdetermination the surface HIE and interior HIE are solved simultaneously to enforce the finding of the unique surface solution.

Table I. Parameters of the studied flames; fuel: hydrogen/nitrogen ratio, D: nozzle diameter, U_{jet}: flow velocity, U_{coflow}: coflow velocity, Re: Reynolds number, f_{stoic}: stoichiometric mixture fraction.

	HD	H3
fuel [vol%]	23/77 H_2/N_2	50/50 H_2/N_2
D [mm]	8	8
U_{jet}	36.3	34.8
U_{coflow}	0.2	0.2
Re	16000	10000
f_{stoic}	0.583	0.310

3. Numerical Simulation of the HD- and H3-flames

3.1. Flame configuration

The flame model is a turbulent, hydrogen, non-premixed, jet flame, combusting a mixture of H_2 and N_2. In the course of our investigations, two different flames were examined. The parameters of the two flames, referred to as HD and H3, are listed in Table I.

The flames differ mainly in the mixture ratio. While the mixture ratio of the H3-flame is 50/50 vol% H_2/N_2, the HD-flame is characterized by a highly diluted mixture of 23/77 vol% H_2/N_2. The fuel was diluted in order to slow down the chemical reactions, i.e. to stabilize the numerical simulation. Due to the high dilution, the HD-flame burns close to its blow-off limit. The circular nozzle diameter is $D = 8$ mm and the fuel discharges with a bulk velocity of $U_{\text{bulk}} = 36.3$ m/s and 34.8 m/s respectively into air coflowing at $U_{\text{coflow}} = 0.2$ m. The corresponding Reynolds numbers are 16000 for the HD-flame and 10000 for the H3-flame. The flames were numerically and experimentally investigated in detail at the Technical University of Darmstadt [29, 30]. The H3-flame is a well studied benchmark flame, defined for the Second International Workshop on Measurement and Computation of Turbulent Non-Premixed Flames [31]. For this flame a detailed documentation can be found on the Internet [32].

3.2. Large-Eddy-Simulation of the source region

The Large-Eddy-Simulation (LES) was executed on a cylindrical computational domain of 48 nozzle diameters D length and a diameter of $27D$ for the HD-flame and a somewhat larger domain of $62D$ length and $32D$ diameter for the H3-flame. The numerical grid consisted of 257 × 32 × 60 (axial × circumferential × radial) cells for the smaller domain and 513 × 32 × 60 cells for the larger domain respectively. The used numerical method assumes that the density is independent of pressure (incompressibility), which is a widespread approximation within the

Table II. Details of the acoustical models for the HD- and H3-flame.

cylinder	radius (cm)		length (cm)		number of nodes		number of elements		maximum frequency (kHz)	
	HD	H3	HD	H3	HD	H3	HD	H3	HD	H3
1	5.34	5.16			1442	1922	1472	1952	4.8	>5
2	5.81	5.75			1442	1794	1472	1824	4.8	5
3	6.32	6.39			1346	1698	1376	1728	4.3	4.8
4	6.85	7.08			1346	1538	1376	1568	4.3	4.5
5	7.42	7.84	38.25	49.90	1250	1442	1280	1472	3.8	4.0
6	8.03	8.66			1186	1346	1216	1376	3.5	3.8
7	8.67	9.55			1122	1250	1152	1280	3.2	3.5
8	9.35	10.5			1058	1186	1088	1216	3.0	3.1
9	10.08	11.58			1026	1122	1056	1152	2.7	2.8
10	10.85	12.73			994	1058	1024	1088	2.5	2.5

methods of computational fluid dynamics for the considered low Mach number flow.

The outputs of a LES are usually mean and standard deviations of different quantities of the flow field as axial or radial distributions of velocity, mixture fraction or temperature. The fluid dynamic properties of the numerical results agree very well with experimental data. Corresponding evaluations are published in [33] and [34]. For our purpose an extraction of instantaneous data is needed. Hence, a data sample at time steps of every 10^{-4} s was generated out of the LES run, which includes the velocity data in x-, y-, z-direction, density, temperature and mixture fraction at selected spatial points of the LES grid.

The LES-code was developed at Technical University Darmstadt, Institute for Energy and Power plant Technology. More detailed information about the used LES-model for turbulent diffusion flames can be found in [29, 35, 33].

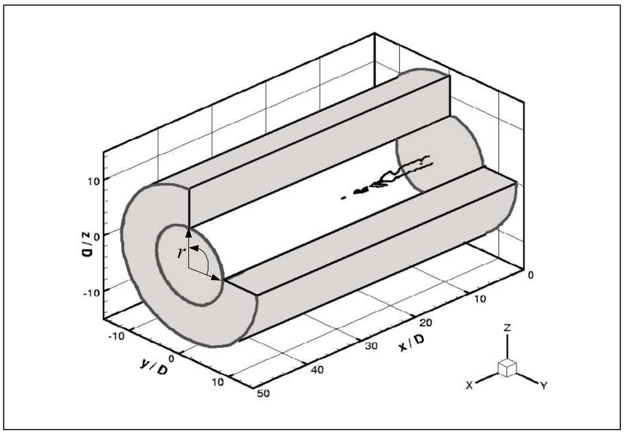

Figure 1. Computational domain of the LES. The instantaneous physical data are sampled in the grey area. The spatial extent of the flame is outlined by the isoline for the stoichiometric mixture fraction of the flame.

4. Pre-processing for BEM and ESM

4.1. Calculation surfaces and FE models

The geometrical grids as well as the calculated physical data were extracted from the Large-Eddy-Simulation. In Figure 1 the total computational domain is shown. For the acoustic calculations, the velocity samples as well as the grid data are taken from the grey area (interface region). From the grid data, extracted out of the interface region, ten cylindrical Kirchhoff surfaces were assembled.

The staggered LES grid has different resolutions in the three different spatial coordinates. While the grid resolution in axial and radial direction is very high, a rather coarse resolution in tangential direction can be found. The maximum distance of the surface nodes determines the frequency range where the Kirchhoff approach is valid. A non-uniform surface mesh leads to an increase of computational costs without an increase of accuracy. Therefore the LES grids were coarsened in axial and radial directions until the resolution met the tangential resolution and the assembling of uniform quadratic surface elements was possible. Figure 2 illustrates this mesh generation.

Random samples have shown that the velocity distribution on the lateral surface area is sufficiently smooth. Thus,

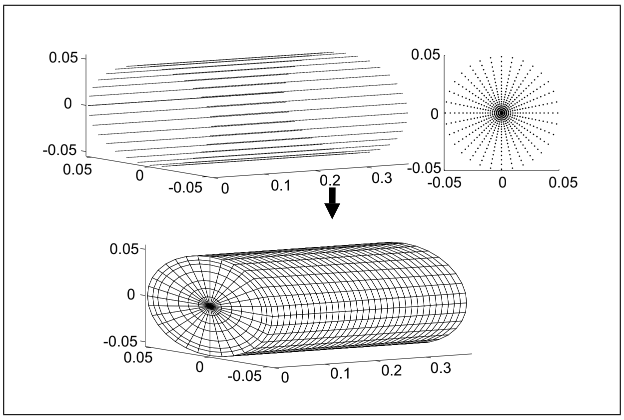

Figure 2. Generation of an equidistant acoustical surface mesh (below) from the grid points of the LES (above).

an aliasing effect is not expected to occur by this spatial down-sampling. However, possible aliasing effects were avoided by averaging the values of adjacent nodes, which represents a low pass-filtering of the spatial distribution. The quality of the filtering and its effect on the final sound

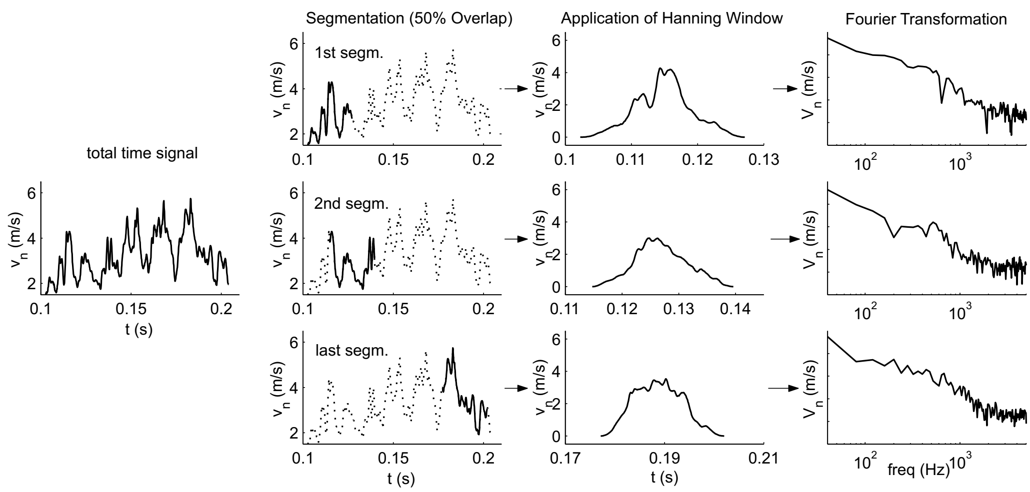

Figure 3. Schema of the computation of the velocity spectra.

radiation shall be thoroughly investigated in a following paper.

From the LES grid data, ten concentric cylindrical surface meshes with increasing radii could be built, so that acoustical simulations on the basis of different enveloping surfaces were possible. A detailed list of the properties of the acoustical models for both flames can be found in Table II. The maximum frequency determines the frequency limit for the validity of the model with respect to the six-elements-per-wavelength rule.

4.2. Input velocity data

As acoustical input data, samples of the flow velocity in x-, y- and z-direction at every node in the interfacing region around the flame were gathered at every 10^{-4} s during the LES run. The original time steps of the LES are in the range of 10^{-6} s. The time step for the data sampling of 10^{-4} s was chosen to establish a frequency range of [0–5000] Hz, which should cover the spectral radiation of the flames. The instantaneous data were directly written out without any low pass-filtering. For the HD-flame a total number of 1717 velocity samples at every spatial point were collected, for the H3-flame even longer time signals of 2619 samples were generated. From the velocity in the three spatial directions, the normal velocity on the control surfaces was calculated. Since only one time series was provided and the power spectrum of the whole signal involves a high variance, the time series was split into sets of 250 samples, so that each set was used as the input velocity for one sound field calculation. The predicted sound power and sound pressure level in the far field are the average over all these individual calculations (see section 6.2). To increase the number of individual sets and therefore decrease the variance of the averaged spectrum, overlap between adjacent segments was considered. According to Welch [36], a 50% overlap along with the use of a Hanning window reduce the aliasing effects as well as keep the dependence between segments in a low level. In Figure 3, the

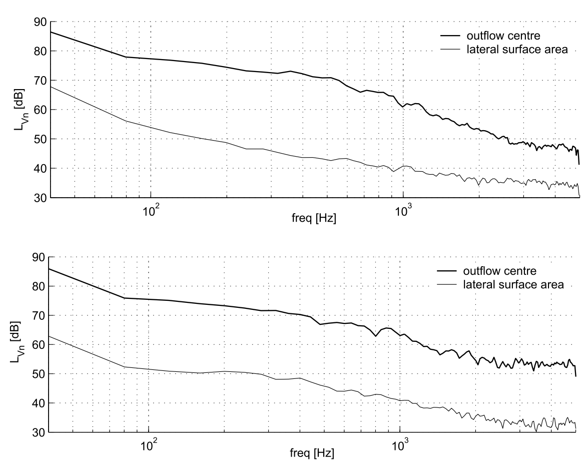

Figure 4. Velocity spectra at the lateral area of the cylindrical control surfaces and near the outflow centre for the HD- and the H3-flame respectively.

procedure to compute the velocity spectra is shown. As a result of the segmentation, the frequency resolution is decreased. For the following calculations, each segment had 250 time samples and the time step was 10^{-4} s. Those parameters give a frequency resolution of 40 Hz and a maximum frequency of 5000 Hz.

The spatial distribution of the normal velocity on the control surfaces shall be illustrated by Figures 4 and 5. Figure 4 shows the averaged spectra of the normal velocity L_{Vn} for a point at the lateral surface area of the tenth cylindrical control surface and for a point near the centre at the outflow cap for both, the HD- and H3-flame.

$$L_{vn} = 20 \log \frac{\overline{v}_n}{v_0}, \quad \overline{v}_n^2 = \frac{1}{N} \sum_{i=1}^{N} \left| v_n^{(i)} \right|^2, \quad v_0 = 10^{-8} \text{ m/s}. \tag{8}$$

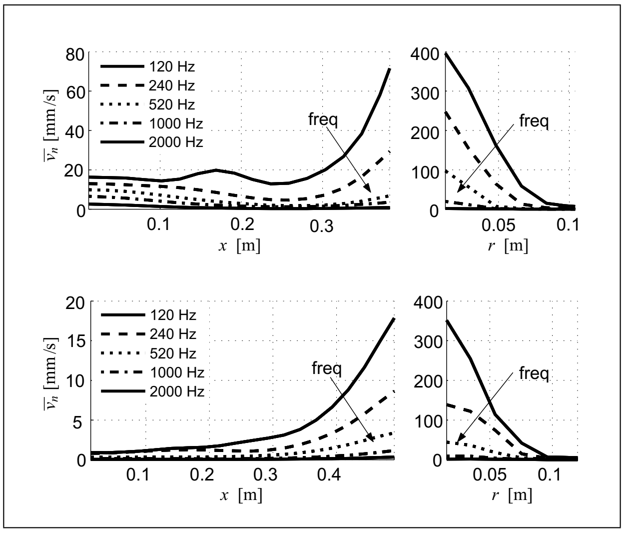

Figure 5. Distribution of the mean normal velocity amplitude on the lateral surface area along the x-axis (left) and on the outflow cap along the radius r (right) for the tenth control surface of the HD- and the H3-flame for different frequencies.

The spectra do not show any distinct narrowband components or other remarkable characteristics. A continuous decrease of the velocity amplitude towards higher frequencies can be observed. Generally, the amplitudes on the outflow cap are much higher than those at the lateral surface.

The graphs in Figure 5 show the distribution of the mean normal velocity $\overline{v}_n$ on the tenth control surface for the HD- and H3-flame. In the left panels the velocity is plotted on the lateral surface area along the x-axis for fixed y- and z-coordinates, the right panels show the velocity distribution along the radius r for a fixed angle θ (see Figure 1) on the outflow cap. Both the velocity distribution on the lateral surface area and on the outflow cap show a high rotational symmetry, therefore the graphs are representative for the velocity distribution on the complete control surface. On the lateral surface area the amplitude increases in direction of the flow. On the outflow cap it decreases with increasing distance from the centre until it meets the velocity amplitudes on the lateral surface area. The highest amplitudes can be found near the centre of the outflow cap. The general decrease of the velocity amplitude can be clearly recognized in the graphs. The velocity on the inflow cap was set to zero because at this side, the adjacent burner represents a rigid boundary condition.

5. Acoustic benchmark data for the HD- and H3-flames

In order to validate the results of the simulation, the sound power of the two investigated flames was experimentally determined. The jet burner was located in a facility without acoustic treatment, for this reason intensity measurements were preferred to pressure measurements to determine the sound power. The radiation patterns were not measured since free field conditions were not fulfilled. The jet flames were thin and long so that the temperature did not represent a problem at all. Only at the top of the flame, a few centimeters away from the flame axis, the sound intensity could not be measured. Figure 6 shows a sketch of the measurement grid and the burner, which was placed on a reflecting surface.

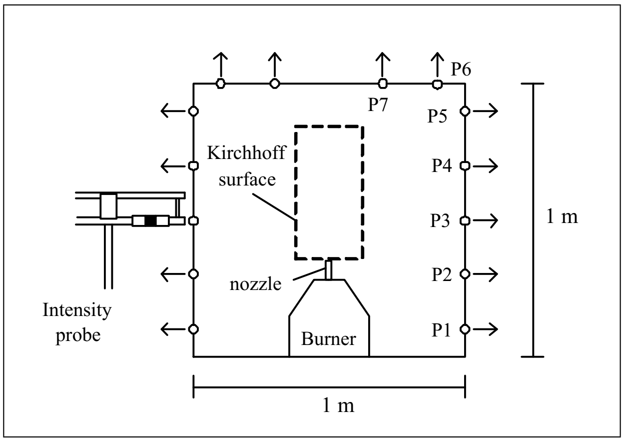

Figure 6. Sketch of the measurement points.

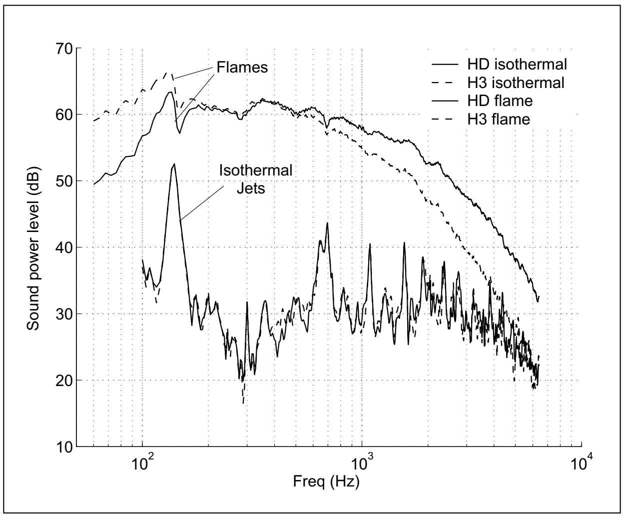

Figure 7. Comparison of the sound power of isothermal jets and flames.

The measurements were made in the afternoon after all activities in the laboratory had finished and all other equipments were switched off in order to avoid the presence of disturbing sound sources. A measurement of the background noise was made and it was well below the flame noise above 100 Hz. A first test measurement confirmed the axial symmetry of the sound, so the number of measured points was reduced to 28. The points were located at a cylindrical surface with radius $R = 0.5$ m and length $L = 1$ m surrounding the burner. Five points parallel to the axis (P1–P5) at $r = R$ and $x = 0.1, 0.3, 0.5, 0.7, 0.9$ at four different angles $\theta = 0°, 90°, 180°, 270°$ and two points at $x = L$ and $R = 0.2, 0.4$ (P6 and P7) at the same angles were used (see Figure 6). The sound intensity normal to the cylindrical surface was measured using a p–p intensity probe connected to a Dual-Channel FFT Analyzer (B&K 2032). The spectra were calculated

Table III. Definition of the parameters used to compare the equivalent source distributions.

Relative surface error F_{rel}	Condition number κ	Sound field error E_f	Sound power level error E_W
$\int_S \lvert v - v_{nS}\rvert^2 \mathrm{d}S \Big/ \int_S \lvert v_{nS}\rvert^2 \mathrm{d}S$	$\lVert A\rVert\,\lVert A^{-1}\rVert \quad (\lVert\,\rVert = \text{norm})$	$\text{median}\left[\left\lvert 20\log_{10}\frac{\lvert p(x)\rvert}{\lvert p_{\mathrm{BBM}}(x)\rvert}\right\rvert\right]$	$L_W^{(\mathrm{ESM})} - L_W^{(\mathrm{BEM})}$

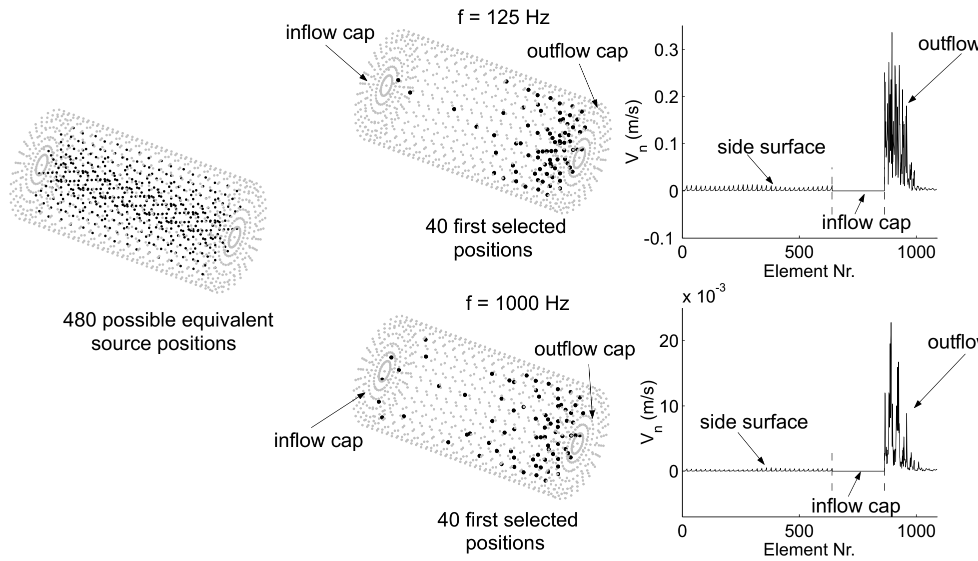

Figure 8. Comparison of the values of the parameters from Table III for optimized and not optimized source positions.

with a Hanning window and averaged during 5 seconds. The measurements were made within two days. The first day, the separation between the microphones in the intensity probe was 12 mm, which allows a frequency range from 500 Hz to 5000 Hz and the second day the separation was 50 mm which gives a frequency range from 100 Hz to 1000 Hz. A comparison of the spectral density obtained with those measurements showed that the measurement with the 12 mm spacer was valid down to 100 Hz and also that the spectra of both series of measurements were reproducible.

The spectra of the sound power of the corresponding isothermal jets without combustion (non reactive flows) and the flames (reactive flows) are illustrated in Figure 7. There are several details that can be observed in these plots. The differences in sound power level between reactive and non reactive cases can be clearly seen. Between 100 Hz and 1000 Hz, the sound power level produced by the combustion is about 20 dB higher.

The spectra of the turbulent jets have a distinct maximum around 140 Hz and many other maxima while the spectra of the flames show a broadband noise. This indicates that the principal mechanisms of sound generation are different for reactive and non reactive flows. The shapes of the spectral curves of both flames are similar because they use the same fuel gases (but with different concentrations) and have nearly the same exit velocity. The sound power increases at low frequencies up to about 136 Hz, then it has a relatively constant value between 150 Hz and 700 Hz, and for frequencies higher than 700 Hz a steady decay follows. The HD-flame shows a steeper increase of the sound power at low frequencies while the decay at high frequencies is less steep than that of the H3-flame. Differences in the sound spectrum of diffusion flames due to different fuels and other parameters have been already reported in [37, 38].

The measured spectra of the HD- and H3-flames are used to validate the ESM and BEM simulations.

6. Results

6.1. Determination of the Equivalent Sources

The number, position and order of the multipoles must be selected in a suitable way. There is no general criterion to choose these parameters. It depends on the type of problem being investigated. The accuracy of the results increase with the number of equivalent sources, but this number cannot be indefinitely unlimitedly raised because the involved matrix becomes ill-conditioned. In this case, a regularization method has to be employed to obtain an approximate solution. Two possible methods that are frequently used are the Truncated Singular Value Decomposition (TSVD) and the Tikhonov Regularization, which define the solution vector in terms of the eigenvalues of the matrix. Numerical tests have been performed [39] and it has been found, that the position of the equivalent sources are only significantly important when monopoles (zero order) are used, but when the order of the multipoles is increased to one or two, a uniform distribution of the sources inside the control surface is sufficient to provide reasonable results. Different equivalent sources distributions have been compared in [39] using the parameters listed in Table III.

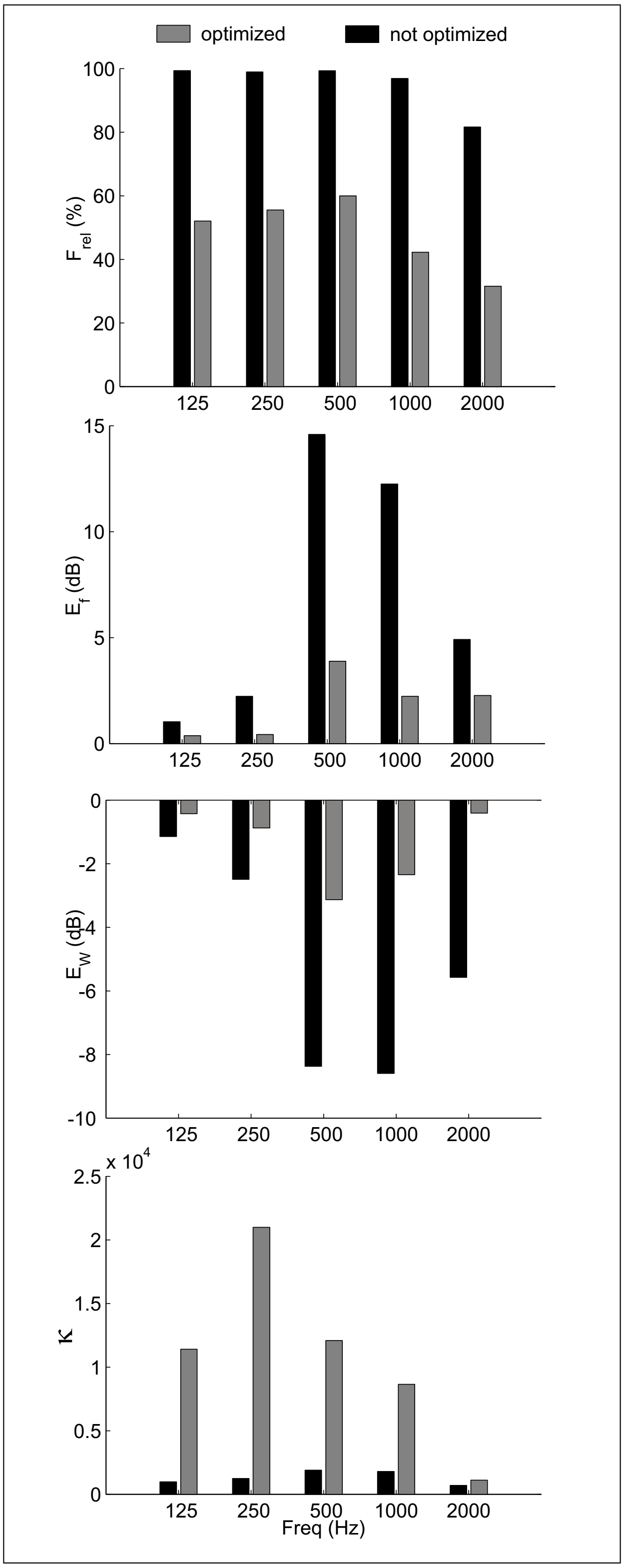

Figure 9. Comparison of results with optimized and not optimized locations.

In Table III, v is the normal surface velocity produced by the multipoles, v_{nS} the known normal surface velocity, A is the matrix resulting from the equations system (see section 2.1), $p(x)$ is the sound pressure at field points and L_W the sound power level. The errors E_f and E_W are computed considering the BEM results as a reference solution.

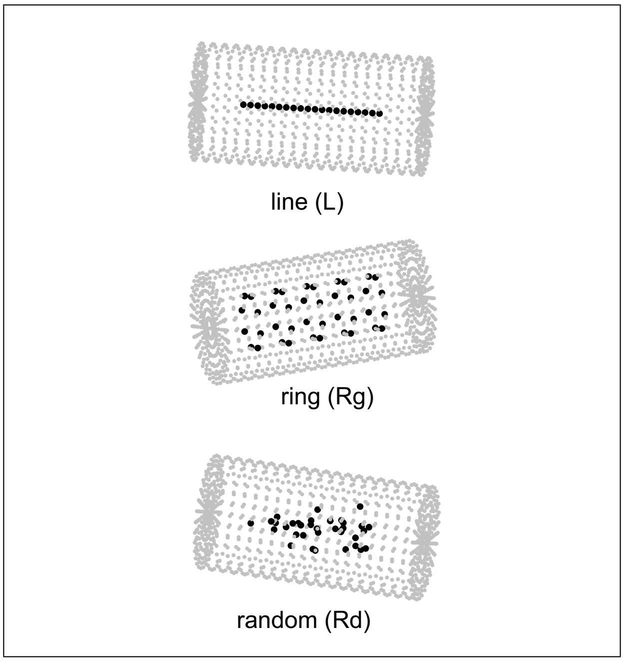

Figure 10. Three different equivalent source distributions.

The optimal positions of the monopoles have been found using an iterative method conceived by Pavic [22]. In this method, a large number of predetermined positions inside the body are selected as possible source positions. One monopole is then considered. From all the source positions, the position which gives the least error is taken and a "rest velocity", defined as the difference between the given velocity and the one obtained with the first monopole, is generated. Once the first position is fixed, a second monopole is moved over the remaining possible positions and the position which best reproduces the rest velocity is taken. The amplitude of the two "optimized" monopoles is then again determined and a new "rest velocity" is calculated. A third optimized position is looked for in the same way, then a fourth and so on until a certain number of monopoles (which is normally lower than the total number considered) is completed. With this procedure, the error at the surface is minimized for a desired number of equivalent monopoles. The selected positions change from frequency to frequency, according to the boundary condition. In Figure 8, all potential positions are shown as well as the first 40 selected positions at 125 Hz and 1 kHz. It is interesting to see that most of the monopoles lie near the upper cap of the cylinder, where the velocity distribution has the highest value. This procedure implies, however, an increase in the computation time, especially if several spectra have to be calculated and averaged for each frequency.

The importance of the source location when using only monopoles is shown in Figure 9. Here, the values of the four comparison parameters of Table III are plotted at five frequencies for optimized and not optimized source posi-

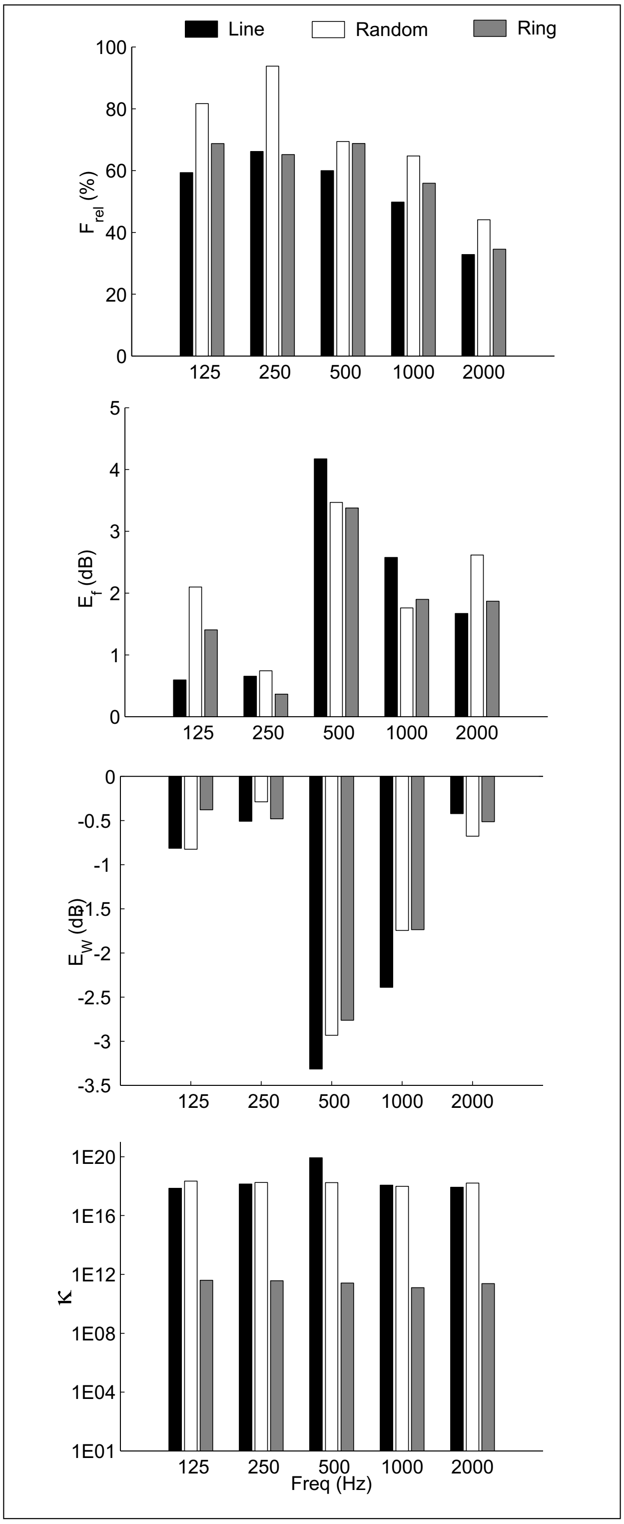

Figure 11. Comparison of the results of three different equivalent source distributions of Figure 10.

tions. The black bars correspond to the results obtained with a set of 40 monopoles placed in the positions labeled as "ring distribution" in Figure 10 and the grey bars correspond to the results provided by 40 monopoles placed in the optimized positions found using PavicŠs method. The results with optimized positions have errors (F_{rel}, E_W and E_f) noticeably smaller than those of the not optimized case, only the condition numbers (κ) are bigger, because the monopoles are closer to each other.

Calculations with equivalent sources of higher orders, distributed inside the control surface, are less sensible to the choice of the source positions. One monopole, three dipoles and five quadrupoles were placed at each source position in all three source distributions of Figure 10 and the results are presented in Figure 11. The differences between source distributions are not very distinct, and vary from frequency to frequency. According to these results, none of the distributions has a definitive advantage over the others, but the ring distribution has the smallest condition numbers. Looking at the surface error (F_{rel}), one finds values varying from 35% up to 60%. These values are high but do not necessarily mean that the radiated sound field will be wrong. An instationary velocity like the one obtained from a turbulent flame has components with spatial wavelengths smaller than wavelength of the fluid that does not radiate but are necessary to reproduce the velocity at the surface.

For the comparison of the sound power curves in the next section, the results of the ring distribution are taken.

6.2. Comparison between ESM, BEM and measurements

The sound radiation of the diffusion flames was calculated with the ESM and BEM using the velocity at the surfaces of the ten cylinders enclosing the flame. Both methods assume that the medium is homogeneous and without flow outside the cylindrical control surface, i.e., the sound field satisfies the homogeneous Helmholtz equation. These conditions are not fulfilled close to the flame, but with increasing distance the flow velocity decreases. Hence, it is expected that the results will reach the real values if the surface is chosen far away enough from the flame. In order to study the dependence of the acoustical quantities on the distance between the control surface and the flame, the sound power and radiation patterns were calculated using concentric cylinders with increasing radii.

The sound power is calculated by integrating the acoustic intensity over a closed surface surrounding the flame. For simplicity, the control surface itself was used to compute the sound power, since the pressure p and velocity v_n at this surface are determined by the calculations.

$$P = \frac{1}{2} \oint_R \Re\left\{ p v_n^* \right\} \mathrm{d}S. \tag{9}$$

Here, $\Re\{\ \}$ denotes the real part of the quantity in brackets and v_n^* is the complex conjugate of v_n. The normal velocity v_n is known from the LES, whereas the pressure p is computed by the ESM and BEM, respectively.

For each velocity spectrum (see section 4.2) a radiated sound field is computed and the resulting sound field is obtained by averaging all calculations.

$$P_{\text{avg}}(f) = \frac{1}{N} \sum_{i=1}^{N} P_i(f). \tag{10}$$

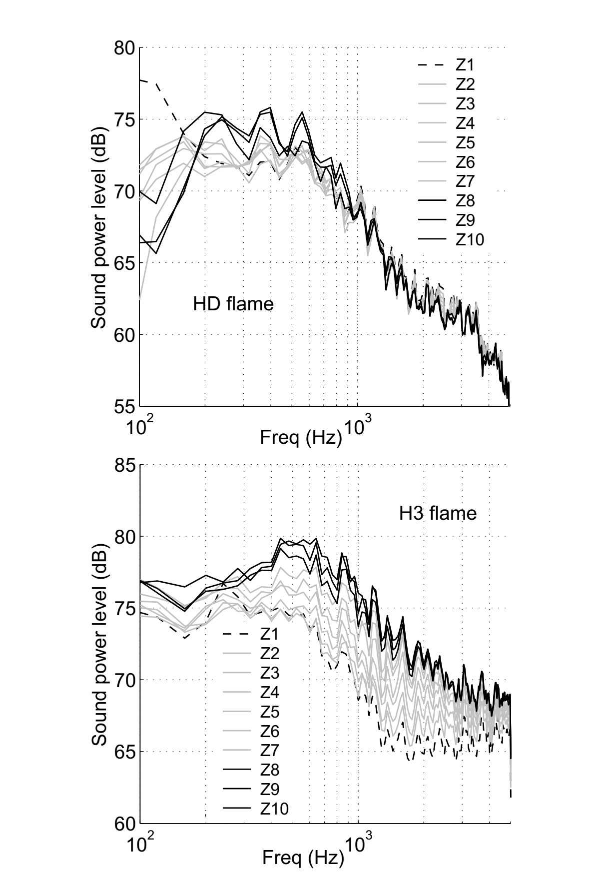

Figure 12. Sound power curves calculated with each of the ten cylinders.

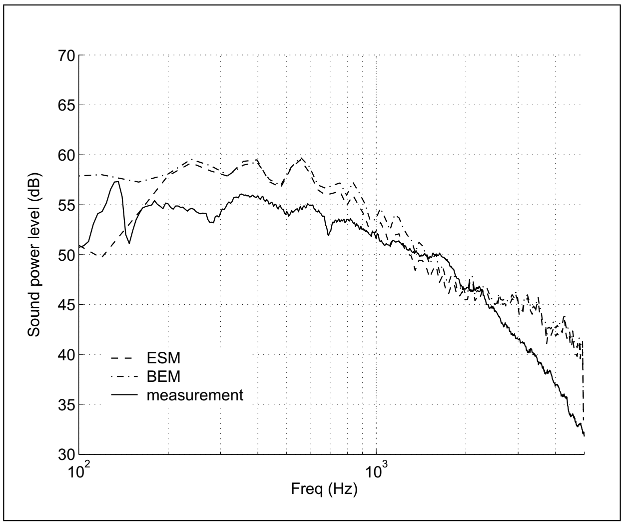

Figure 13. Simulated and measured sound power level of the HD-flame.

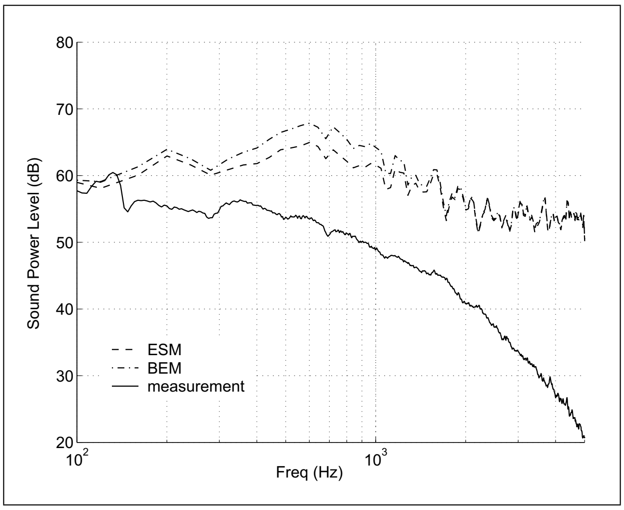

Figure 14. Simulated and measured sound power level of the H3 flame.

The cylindrical control surfaces used to compute the sound power have the same length but different radii. In case of the HD-flame, the length of the cylinder was 38.3 cm and the radii varied from 5.3 cm to 10.8 cm. The cylinders for the H3-flame were 50 cm long and the radii varied from 5.0 cm to 12.7 cm.

In Figure 12, the curves of the sound power are compared. It can be seen that for the HD-flame, the curves are practically the same above 1000 Hz. Below that frequency, there are differences but a certain convergence could be found for the last two cylinders (Z9 and Z10). The situation is different in case of the H3-flame. The convergence only occurs for the last three cylinders over the whole frequency range. According to the above results, the curves calculated with the tenth cylinder are used in both cases for the comparison between simulated and measured sound power.

In Figures 14 and 15 the sound power of both flames, obtained from the simulations of the ESM and BEM are compared with the measurements.

The results of the ESM and BEM are very similar in both cases. In case of the HD-flame, there is a noticeable difference below 100 Hz, probably because of the high condition numbers of the matrix that must be inverted to determine the strength of the equivalent sources. Above 100 Hz, the difference is not bigger than 2 dB. For the H3-flame, the differences are also small over all frequencies, with a slight increase at the mid frequencies between 500 Hz and 1 kHz.

The agreement between simulations and measurements is different for the two flames. The shape of the simulated curves of the HD-flame agrees well at frequencies below 1 kHz but the amplitude is about 3 dB overestimated. Above 1 kHz, the slope of the decay differs a little from the measured decay. For the H3-flame, the results are not as good as for the HD-flame. The overestimation of the calculated sound power reaches 9 dB and also the decay of the curve at higher frequencies is not well reproduced.

In order to explain the discrepancies observed for the H3-flame, the spectra of the sound intensity were compared at some of the measurement points. The sound power is a global quantity because it involves integration of the intensity over a surface surrounding the source region and it is much less sensitive to the environment when determined using the intensity measurement technique.

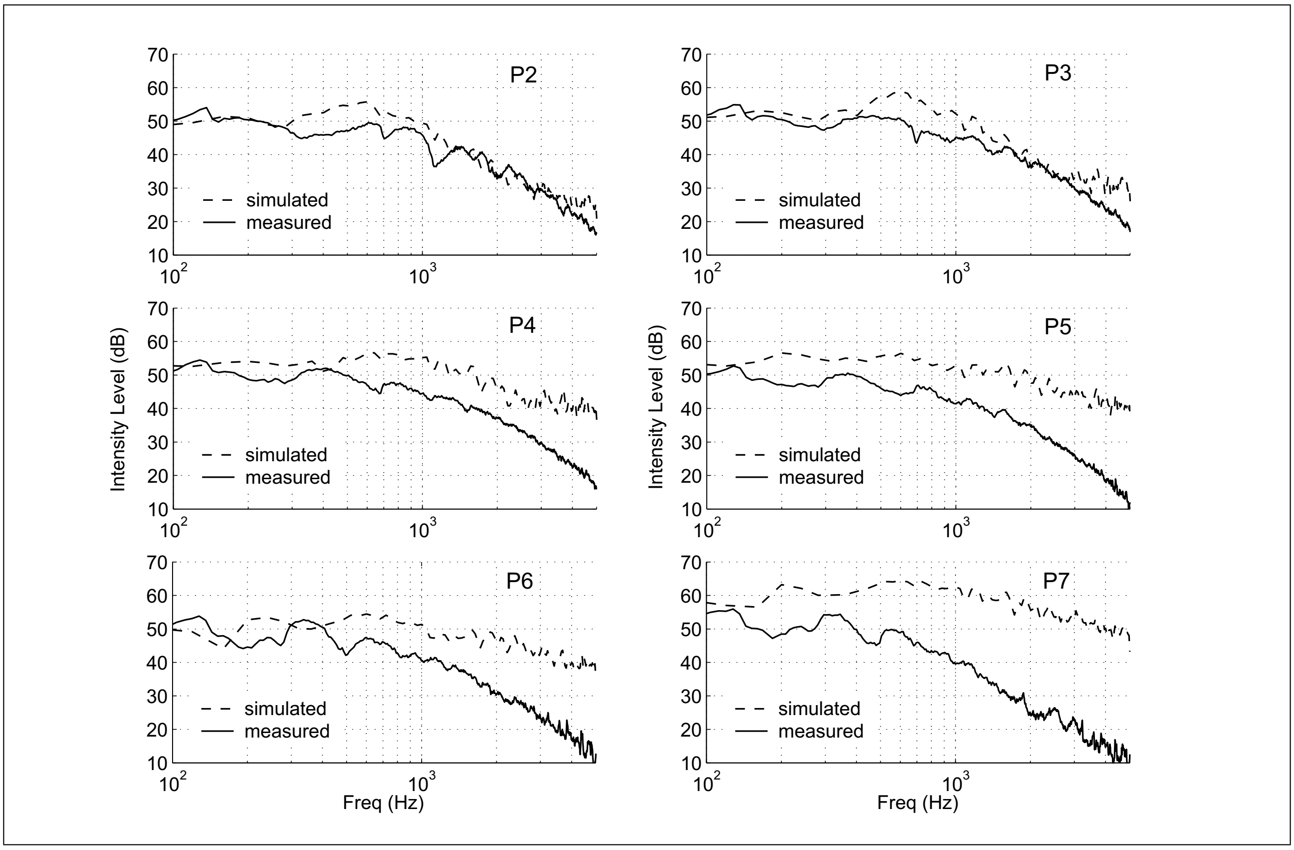

Figure 15. Comparison of simulated and measured sound intensity at points P2-P7 around the flame (The location of P1-P7 are shown in Figure 6).

The measured intensity contains also the reflected waves, but in a region near the source, the direct sound dominates over the reverberant sound and a quantitative comparison of measured and simulated intensity is possible.

The plots of the sound intensity in Figure 15 show that the simulated field at points located on the side of the flame agrees well in level and shape with the measured one. The simulated intensity spectra show an increased level at high frequencies at side points near the top (P4 and P5) and at the top (P6 and P7). Because the simulated intensity spectrum does not decay with the same slope as the measured one at points near the outflow axis, the deviations can grow significantly at high frequencies. This occurs especially at P6 and P7, but these points are closer to the outflow cap than the others and hence more strongly influenced by the cap. This comparison indicates that the largest contribution to the total sound power in the simulation is given by the outflow cap of the cylinder. This presumption is verified when the portion of the sound power of the outflow cap is calculated separately from the rest of the cylindrical surface (see Figure 16).

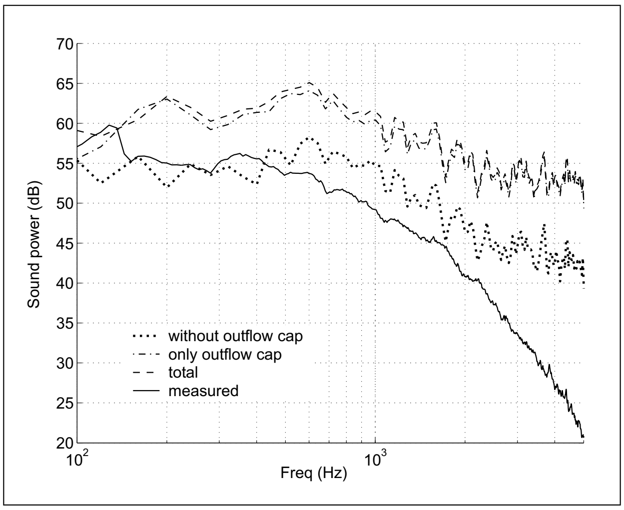

Figure 16. Contribution to the sound power from upper cap and rest of cylindrical surface.

From the analysis of the results, it is evident that the acoustic calculations are affected by the strength of the velocity near the flame axis which may contain a non radiating component that has not yet died down. We suppose that this effect is also responsible for the overestimation of the sound power of the HD-flame. However, in that case it is not too strong because this flame is shorter and the selected cylinders are large enough, so that at their outflow cap, the turbulent components may have decreased. The above results enhance the critical role that the position of the Kirchhoff surface plays in the accuracy of these methods.

6.3. Directivity patterns

As mentioned before, the directivity patterns of the flames were not measured, since the jet burner was placed in a room without acoustic treatment. Therefore the directional properties of the simulated sound could not be compared with experimental values.

A comparison between the directivities computed by the ESM and the BEM shows that they are, like the sound power, very similar (Figure 17). Differences vary from one frequency to the other but remain always small.

The polar plots show the dependence of the directivity on the frequency. At low frequencies, the sound radiation is uniform in all directions, but it becomes more focused towards the direction of the outflow by increasing frequencies. This behavior is expected since the outflow cap of the cylinder was identified as the most important radiating surface. The radiated sound is also symmetric around the flame axis.

7. Discussion

The comparison between the results obtained with our particular hybrid method and experimental results shows a reasonable agreement for the HD flame but distinct deviations of the spectral sound power for the H3 flame, especially at high frequencies. The error was shown to be originated by an overestimation of the velocity at the outflow cap of the cylindrical control surface. As factors that can contribute to this overestimation, we can mention the aliasing effects due to time and space sampling, the short duration in real time of the velocity signal, the use of an incompressible LES code for the near field prediction and the contribution of vortical structures of the flow to the velocity distribution at the outflow cap.

Possible aliasing effects, due to the down-sampling in the time domain, could have lead to an overestimation of the velocity amplitude in the higher frequency range. A data sampling with a preceding low pass-filtering and its effect on the velocity spectra will be studied in the near future.

The length of the available time signals depends strongly on the computing time of the LES. The total 0.2 seconds, which is the length of the velocity series, took more than a month. The given length of the time signal does not allow a proper averaging of the spectra.

The third factor is related to the type of flames that were simulated. The LES code does not couple density and pressure. Density fluctuations, which are considerably high in the combustion zone, are nevertheless considered. For the low Mach numbers of the flow, this approximation allows saving computational costs and gives a satisfactory representation not only of the flow mean quantities, but also of the chemical characteristics. Measurements of flow mean quantities on the H3-flame, have confirmed this assumption [33]. The "incompressibility" assumption brings some advantages for the dynamic and chemical description of the flow, but has an effect on the accuracy of the acoustical representation of the flow, when using a hybrid method

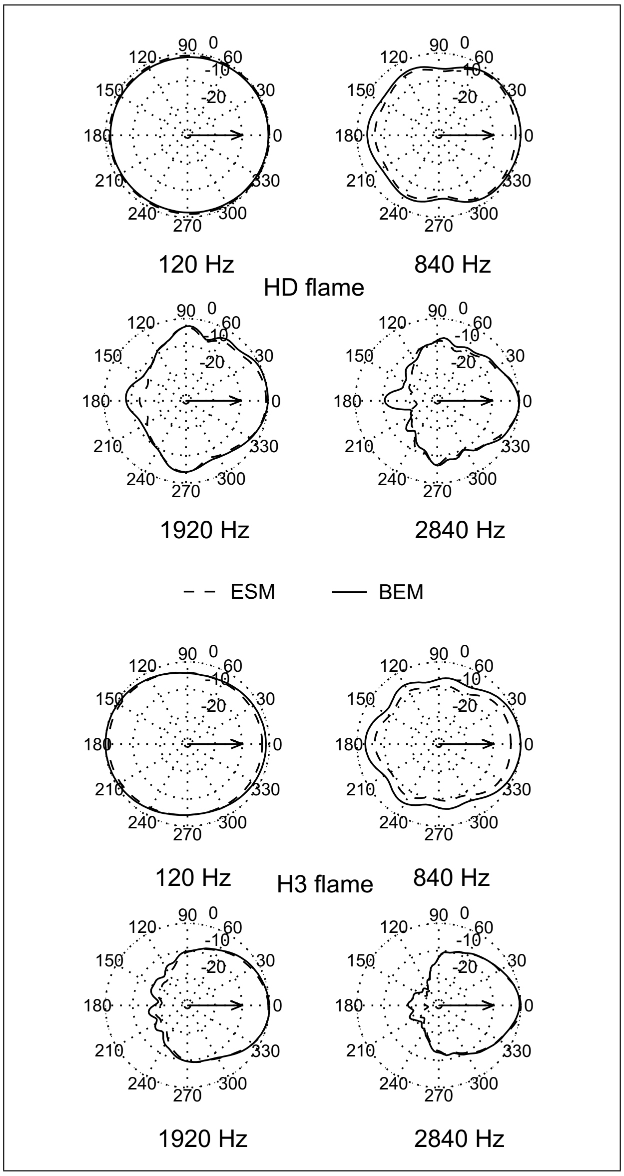

Figure 17. Directivity patterns of both flames at four different frequencies. The arrows indicate the direction of the gas outflow.

like the one shown in the present work. The use of the incompressible velocity data as input to the acoustic methods is questioned under the idea that these data do not contain "acoustic information" (the data from a compressible calculation would), but it should be remembered that in case of vibrating bodies, the normal velocity of the body surface is used as input to the same acoustic methods, and we do not need to differentiate between acoustic and non-acoustic components. This aspect is expected to be better investigated in the future when a compressible calculation is available.

Difficulties to define a closed surface enveloping a jet and lying in a homogeneous medium in order to perform a surface-integral-technique are known. A usual practice to avoid this problem is to utilize open control surfaces [2, 3, 4]. According to Freund [40], the sound field can still be well predicted using open surfaces at field points which are not located near the axis of the jet. In our case, since only the normal velocity at the control surface is known, the surface must be closed in order to obtain a unique solution of the problem. Therefore, in our method, the velocity at the outflow cap must be included and correctly determined. Techniques to separate radiating and non-radiating components of the velocity are still being developed. How far recent approaches to remove the hydrodynamic part of the flow on the outflow cap as published in [41] can be applied to the present method is currently under examination. It is expected, that passing vortical structures induce a high velocity level at the outflow cap and that the elimination of these vortical perturbations will improve the accuracy of the velocity boundary condition for the BEM and ESM.

8. Summary

A hybrid method that couples a Large Eddy Simulation (LES) with the ESM or the BEM has been used to determine the radiated sound of two open non-premixed jet flames. The coupling of both methods is carried out on a cylindrical Kirchhoff surface that encloses the flame. The coupling variable is the velocity calculated by the LES which serves as boundary condition for the ESM/BEM. For the calculation of the sound radiation, acoustic meshes must be generated using the coordinates of the LES points and the velocity time series converted from the time to the frequency domain. The sound power and directivity patterns of the flames computed by the ESM and the BEM agree very well. The sound power of the simulated flames was also experimentally determined and used to validate the results of the method. The agreement between simulated and measured curves is quite good for the HD-flame in a wide frequency range with a slight overestimation around 3-5 dB. The simulation of the H3-flame shows a distinct overestimation of the sound power level of more than 10 dB above 500 Hz.

The particularly simple coupling of the LES and the ESM/BEM shows promising results at least in the lower frequency range and it has the potential to be further developed as a useful tool for the determination of the sound radiation of open flames.

Acknowledgement

We thank Prof. Janicka and Mr. Flemming from the TU Darmstadt for the cooperation and for providing the data of the LES calculations. We also thank Mr. Richter from the TU Dresden and Mr. Nauert from the TU-Darmstadt for the support during the measurements. This work is integrated in the research unit “Combustion Noise Initiative”, supported by the German Research Foundation (DFG), [42].

References

[1] A. Lyrintzis: Surface integral methods in computational aero acoustics – from the (CFD) near-field to the (Acoustic) far-field. International Journal of Aero Acoustics **2** (2003) 95–128.

[2] A. Uzun, A. Lyrintzis, G. Blaisdell: Coupling of integral acoustic methods with LES for jet noise prediction. AIAA-Paper 2004-0517, 42nd Aerospace Sciences Meeting and Exhibit, 2004.

[3] G. Rahier, J. Prieur, F. Vuillot, N. Lupoglazoff, A. Biancherin: Investigation of integral surface formulations for acoustic post-processing of unsteady aerodynamic jet simulations. Aerospace Science and Technologie **8** (2004) 453–467.

[4] N. Andersson, L. Eriksson, L. Davidson: Large eddy simulation of subsonic turbulent jets and their radiated sound. AIAA Journal **43** (2005) 1899–1912.

[5] L. Morino, M. Gennaretti, U. Iemma, F. Salvatore: Aerodynamics and aeroacoustics of wings and rotors via BEM - unsteady, transonic, and viscous effects. Computational Mechanics **21** (1998) 265–275.

[6] T. Wood, S. Grace: Time-dependent calculation of acoustic radiation from finite wings using BEM. Proceedings of IMECE 2000, International Mechanical Engineering Congress and Exposition, Orlando, Florida, USA, November 5-10, 2000.

[7] E. Manoha, G. Elias, B. Troff, P. Sagaut: Towards the use of boundary element method in computational aeroacoustics. 5th AIAA/CEAS Aeroacoustics Conference, Bellevue, WA, USA, May 10-12, 1999.

[8] C. Montavon, I. P. Jones, S. Szepessy, R. Henriksson, Z. el-Hachemi, S. Dequand, M. Piccirillo, M. Tournour, F. Tremblay: Noise propagation from a cylinder in a cross flow: comparison of SPL from measurements and from a CAA method based on a generalised acoustic analogy. IMA Conference on Computational Aeroacoustics, University of Greenwich - Maritime Greenwich Campus, April 9–11, 2002.

[9] C. Polacsek, S. Burguburu: CFD-BEM coupling for computing noise radiated from engine inlets. Proceedings Computational Aeroacoustics - Euromech 449, Chamonix, France, 2003.

[10] M. Heckl: Bemerkung zur Berechnung der Schallabstrahlung nach der Methode der Kugelfeldsynthese. Acustica **68** (1989) 251–257.

[11] G. Koopmann, L. Song, J. Fahnline: A method for computing acoustic fields based on the principle of wave superposition. Journal of the Acoustical Society of America **86** (1989) 2433–2438.

[12] M. Ochmann: Die Multipolstrahlersynthese – ein effektives Verfahren zur Berechnung der Schallabstrahlung von schwingenden Strukturen beliebiger Oberflächengestalt. Acustica **72** (1990) 233–246.

[13] L. Song, G. Koopmann, J. Fahnline: Numerical errors associated with the method of superposition for computing acoustic fields. Journal of the Acoustical Society of America **89** (1991) 2625–2633.

[14] R. Jeans, I. Mathews: The wave superposition method as a robust technique for computing acoustic fields. Journal of the Acoustical Society of America **92** (1992) 1156–1166.

[15] M. Ochmann: The source simulation technique for acoustic radiation problems. Acustica **81** (1995) 512–527.

[16] Y. Bobrovnitskii, T. Tomilina: General properties and fundamental errors of the method of equivalent sources. Acoustical Physics **41** (1995) 649–660.

[17] W. Kroop, P. Svensson: Time domain formulation of the method of equivalent sources. Acta Acustica **3** (67-73) 1995.

[18] M. Johnson, S. Elliot: An equivalent source technique for calculating the sound field inside an enclosure containing

scattering objects. Journal of the Acoustical Society of America **104** (1998) 1221–1231.

[19] N. Atalla, G. Winckelmans, F. Sgard: A multiple multipole expansion approach for predicting the sound power of vibrating structures. Acustica united with Acta Acustica **85** (1999) 47–53.

[20] M. Ochmann: The full-field equations for acoustic radiation and scattering. Journal of the Acoustical Society of America **105** (1999) 2574–2584.

[21] Y. Gounot, R. Musafir: Optimization of source positioning and strength in equivalent sources method using genetic algorithms. Proceedings Internoise 2004, Prague, Czech Republic, 2004.

[22] G. Pavic: An engineering technique for the computation of sound radiation by vibrating bodies using substitute sources. Acta Acustica united with Acustica **91** (1-16) 2005.

[23] F. Holste: An equivalent source method for calculation of the sound radiated from aircraft engines. Journal of Sound and Vibration **203** (1997) 667–695.

[24] T. Wu: Boundary element acoustics: Fundamental and computer codes. WIT Press, Southampton, Boston, 2000.

[25] M. Ochmann, F. P. Mechel: Analytical and numerical methods in acoustics. – In: Formulas of Acoustics, Chap. 0. F. P. Mechel (ed.) Springer Verlag, Berlin Heidelberg, 2002, 930–1005.

[26] O. von Estorff: Boundary element acoustics: Advances and applications. WIT Press, Southampton, Boston, 2000. 1-44, 285-316.

[27] S. Marburg: Six boundary elements per wavelength. Is that enough? Journal of Computational Acoustics **10** (2002) 25–51.

[28] H. Schenck: Improved integral formulation for acoustic radiation problems. Journal of the Acoustical Society of America **44** (1968) 41–58.

[29] A. Kempf: Large eddy simulation of non-premixed flames. Thesis, TU Darmstadt, 2003.

[30] M. Tacke: Zur Stabilität angehobener turbulenter Diffusionsflammen. Thesis, TU Darmstadt, 1998.

[31] R. Barlow (ed.) Proceedings of the International Workshop on Measurement and Computation of Turbulent non-premixed Flames, 1997. Available from: http://www.ca.sandia.gov/TNF/ 2ndWorkshop/TNF2.html.

[32] Technische Universität Darmstadt, Institute for Energy and Powerplant Technology, Flame Data Base for Turbulent non-premixed Flames. Available from: www.tu-darmstadt .de/fb/mb/ekt/flamebase/Welcome.html, 1997.

[33] F. Flemming, A. Nauert, A. Sadiki, J. Janicka, H. Brick, R. Piscoya, M. Ochmann, P. KŤltzsch: A hybrid approach for the evaluation of the radiated noise from a turbulent non-premixed jet flame based on large eddy simulation and equivalent source and boundary element methods. Proc. ICSV12, Lisbon, Portugal, 2005.

[34] F. Flemming, A. Sadiki, J. Janicka: Investigation of combustion noise using a LES/CAA hybrid approach. Proc. Comb. Inst. **31** (2007) 3189–3196.

[35] A. Kempf, A. Sadiki, J. Janicka: Prediction of finite chemistry effects using large-eddy simulation. Proc. Comb. Inst. **29** (2002) 1979–1985.

[36] P. D. Welch: The use of the Fast Fourier Transform for the estimation of power spectra: A method based on time averaging over short, modified periodograms. IEEE Transactions on Audio and Electroacoustics **15** (1967) 70–73.

[37] B. Lenze, D. Pauls: Die Entstehung und Bekämpfung von Brennergeräuschen. GWF-Gas/Erdgas **115** (1974) 48–54.

[38] K. Singh, S. Frankel, J. Gore: Study of spectral noise emissions from standard turbulent nonpremixed flames. AIAA Journal **42** (2004) 931–936.

[39] R. Piscoya, H. Brick, M. Ochmann, P. Költzsch: Numerical aspects of the equivalent source method applied to combustion noise. Proc. ICSV12, Lisbon, Portugal, 2005.

[40] J. Freund: Calculation of the radiated sound field using an open Kirchhoff surface. AIAA Journal **34** (1996) 909–916.

[41] M. L. Shur, P. R. Spalart, M. K. Strelets: Noise prediction for increasingly complex jets. Part I: Methods and tests. International Journal of Aeroacoustics **4** (2005) 213–246.

[42] Combustion Noise Initiative.
URL: http://www.combustion-noise.de.